Benchmarking accurate spectral phase retrieval of single attosecond pulses

Hui Wei, Anh-Thu Le, Toru Morishita, Chao Yu, and C. D. Lin

Phys. Rev. A **91**, 023407 — Published 9 February 2015

DOI: 10.1103/PhysRevA.91.023407

Benchmarking accurate spectral phase retrieval of single attosecond pulses

Hui Wei,[1] Anh-Thu Le,[1] Toru Morishita,[2] Chao Yu[1,3] and C. D. Lin[1]
[1] *J. R. Macdonald Laboratory, Department of Physics, Kansas State University, Manhattan, Kansas 66506, USA*
[2] *Department of Engineering Science, The University of Electro-Communications, 1-5-1 Chofu-ga-oka, Chofu-shi, Tokyo, 182-8585, Japan*
[3] *Department of Applied Physics, Nanjing University of Science and Technology, Nanjing 210094, Peoples Republic of China*

A single extreme-ultraviolet (XUV) attosecond pulse or pulse train in the time domain is fully characterized if its spectral amplitude and phase are both determined. The spectral amplitude can be easily obtained from photoionization of simple atoms where accurate photoionization cross sections have been measured from, e.g., synchrotron radiations. To determine the spectral phase, at present the standard method is to carry out XUV photoionization in the presence of a dressing infrared (IR) laser. In this work we examine the accuracy of current phase retrieval methods (PROOF and iPROOF) where the dressing IR is relatively weak such that photoelectron spectra can be accurately calculated by second-order perturbation theory. We suggest a modified method named swPROOF (scattering wave Phase Retrieval by Omega Oscillation Filtering) which utilizes accurate one-photon and two-photon dipole transition matrix elements and removes the approximations made in PROOF and iPROOF. We show that the swPROOF method can in general retrieve accurate spectral phase compared to other simpler models that have been suggested. We benchmark the accuracy of these phase retrieval methods through simulating the spectrogram by solving the time-dependent Schrödinger equation (TDSE) numerically using several known single attosecond pulses with a fixed spectral amplitude but different spectral phases.

PACS numbers: 32.80.Fb, 42.65.Re

I. INTRODUCTION

Since the first report of the generation of attosecond pulse trains (APT)[1] and single attosecond pulses (SAP)[2] in the extreme-ultraviolet (XUV) in 2001, attosecond pulses are becoming essential laboratory tools for probing the dynamics of atoms, molecules and solids. Today attosecond pulses are mainly produced by high-order harmonic generation (HHG) process with intense femtosecond near-infrared (NIR) to mid-infrared (MIR) laser pulses in a gas medium. For applications in science and technology and for the purpose of probing dynamics in the attosecond timescale, it is desirable that single attosecond pulses are routinely generated, with the goal of shorter pulse duration, higher intensity and higher photon energy, especially for the water window and the X-ray region. So far attosecond pulses as short as 80 as [3] and 67 as[4] have been reported. These pulses have central energy below 150 eV. To generate SAP, temporal gating techniques such as polarization gating[5] and double optical gating[6] have already been developed. Recently spatiotemporal gating methods including attosecond lighthouse[7, 8] and noncollinear optical gating[9] have also been introduced[10].

In the past decade, APT and SAP have been used to study dynamics of atoms, molecules and condensed matter. In the experiment, an APT or SAP is used to excite the target in the presence of a near-infrared laser (typically around 800 nm). The dressing laser will modify the medium as well as the wave packet generated by the attosecond pulse, as the delay between the two pulses is varied. Thus wave-packet dynamics such as quantum interference, shake-up, autoionization, a.c. Stark shift, or time delay in photoionization, have been explored in many experiments[11–28], mostly by detecting the electron momentum spectra. Recently, transient absorption spectroscopy has also been used[29–34] in view that better spectral resolution can be achieved by measuring photons. A recent review on experimental activities with attosecond pulses is given by Lepine *et al.*[35].

In spite of a wealth of literature on attosecond pulses in the past decade, precise real-time observation of electron dynamics on attosecond timescale is still very limited since a precise characterization of such pulses in the time domain remains a challenging task[36–41]. The spectral amplitude of attosecond pulses can be easily retrieved from the XUV-only photoelectron spectrum provided that the one-photon ionization cross section of the target is known. Thus the main difficulty in attosecond pulse characterization is the accurate retrieval of the spectral phase. With known spectral amplitude and phase, the attosecond pulse in the time domain is obtained by a simple inverse Fourier transform. Today methods that have been developed for determining the phase of attosecond pulses include streaking, RABITT, PROOF and iPROOF. In attosecond streaking[42] the XUV pulse is converted into an electron wave-packet via photoionization. Due to the presence of the phase-locked dressing IR field, the photoelectron spectrum in a given direction modulates as a function of the time delay between the XUV and the IR pulses. To achieve pronounced modulation, the IR field has to be relatively intense, but not intense enough to ionize the atom by itself alone. Assuming that the strong field approximation (SFA) is accurate enough to describe the electron

spectrum at each time delay[43], the phase of the XUV pulse can be retrieved using the so-called FROG-CRAB method(frequency-resolved optical gating for complete reconstruction of attosecond bursts)[44, 45]. In order to use the standard FROG algorithm, the FROG-CRAB introduces an additional "central momentum approximation", which assumes the bandwidth of the XUV is small compared to its central energy. Many of the time-domain XUV attosecond and IR femtosecond pulses are thus retrieved simultaneously. However, the accuracy of the FROG-CRAB method has never been carefully calibrated. It is well-known that the standard SFA is not an accurate theory for predicting the photoelectron spectra in an intense laser field. Although further derivation beyond standard SFA such as the Coulomb-Volkov approximation[46] can improve the accuracy, the validity of such central momentum approximation is not guaranteed when characterizing a broadband XUV pulse. Yakovlev *et al.*[47] investigated the central momentum approximation by assuming an artificial bound-free transition matrix element that has a sharp minimum, and they found that the FROG-CRAB tends to retrieve a "time-domain wave packet" rather than the XUV pulse. More calibrations using accurate matrix element and broader band XUV pulses are strongly desirable. Such uncertainty in the FROG-CRAB method renders the claims for precise duration of attosecond pulses and the interpretation of time-domain experimental results less trustworthy.

Since accurate theory for retrieving attosecond pulses via strong field ionization is very complicated, it is desirable to retrieve the spectral phase by applying a weak IR field. In the limit that second-order perturbation theory is adequate for describing the photoelectron spectra, the theory is on good footing. Indeed this is how the attosecond pulse trains are characterized[1]. Using the so-called RABITT method (reconstruction of attosecond beating by interference of two-photon transition), the relative phase between two successive odd harmonics (separated by 2ω) can be accurately obtained from the modulation (with frequency 2ω) of the even-harmonic sidebands vs. the time delay. The 2N-th sideband harmonic is generated by absorbing a (2N-1)-th XUV harmonic and an IR photon, or by absorbing a (2N+1)-th XUV harmonic and emitting an IR photon. The amplitudes from the two pathways interfere, thus the phase difference between the two neighboring harmonics is encoded in the spectra and can be retrieved accurately. The RABITT method does not work if the harmonics are separated by ω (generated by an $\omega + 2\omega$ two-color field) nor for a single attosecond pulse where the spectral phase information is encoded in the interference between the first-order term from the XUV alone and two second-order terms involving XUV plus IR processes. A phase retrieval method based on analyzing this first-second-order interference (FSI) term was proposed by Laurent *et al.*[48]. They called their method as iPROOF, which was an improved version of the PROOF method (Phase Retrieval by Omega Oscillation Filtering) proposed by Chini *et al.*[49]. The PROOF method starts with the strong field approximation for describing XUV ionization in a weak dressing IR field. By expanding the SFA equation in the weak field limit, they analyzed the ω-oscillation (instead of the 2ω oscillation in RABITT) due to the first-second-order interference. Since PROOF does not include the atomic structure, this model is not expected to explain the experimental electron spectra. The iPROOF is based on the correct second order perturbation theory and it should be possible to use it to characterize attosecond pulse trains as well as single attosecond pulses. Unfortunately the two-photon transition matrix elements used in iPROOF were calculated with an additional approximation[50, 51] which renders the phase retrieved via iPROOF inaccurate.

In this article, our goal is to benchmark the accuracy of the spectral phase retrieved for single attosecond pulses using PROOF, iPROOF and our swPROOF (scattering wave PROOF) method. The swPROOF takes advantage of accurate atomic transition matrix elements which are calculated by using real scattering wave functions. This method is based on fundamentally correct theory so long that the IR intensity is in the region where second-order perturbation theory is valid. It is the correct counterpart of the RABBIT method which was applied to retrieve attosecond pulse trains. To benchmark the accuracy of the phase retrieval, in the present work we solve the time dependent Schrödinger equation (TDSE) numerically in the presence of a given XUV pulse and a delayed dressing IR field. The computed spectrogram is to serve as the "real" experimental data. The PROOF, iPROOF and swPROOF methods are then applied on this spectrogram to retrieve the spectral phase that can be checked against the actual input XUV spectral phase. The main contribution of this work is that we calculate the two-photon transition matrix elements used in the swPROOF accurately via the Dalgarno-Lewis method[52] without adopting the approximations used in iPROOF. We will show that the swPROOF method indeed improves the attosecond pulse characterization. Note that all the three methods are based on "Phase Retrieval by Omega Oscillation Filtering" (PROOF). The original PROOF[49] could be more correctly represented by such as "pwPROOF" since it uses plane waves to describe continuum electrons, but in the present paper we follow its original name without introducing too many terms.

This paper is organized as follows: Sec.II.A gives a general framework of the spectral phase retrieval from the first-second-order interference (FSI) term in the photoelectron spectra based on the second-order perturbation theory. In Sec.II.B and C we present the evaluation of the one- and two-photon transition dipole matrix elements in details. The approximations used in PROOF and iPROOF are discussed in Sec.II.D. In Sec.II.E the concept of continuum-continuum phase is elaborated since it also enters in the formulation of numerous articles on time delay studies. In Sec.III.A we compare the electron spectra calculated from TDSE with the spectra

from PROOF, iPROOF and swPROOF methods, and we also show the sensitivity of the FSI term to the spectral phase. The results of the pulse characterization are given in Sec.III.B, assuming that the IR intensity is either known or unknown in the retrieval process. In Sec.III.C we study the effect of the dressing IR intensity to identify where the present swPROOF method begins to fail. The conclusions are presented in Sec.IV. Atomic units are used in this paper unless otherwise stated.

II. THEORETICAL METHODS

A. First-Second-order Interference term in photoelectron spectra

Consider a combined XUV pulse and an IR field interacts with an argon atom. Both fields are linearly polarized along the z-axis. The XUV pulse can be described by

$$\begin{aligned} E_{XUV}(t) &= \sqrt{I(t)}\cos(\Omega_0 t+\phi(t)) \\ &= \frac{1}{2\pi}\int_{-\infty}^{\infty}\tilde{E}_{XUV}(\Omega)e^{i\Omega t}\mathrm{d}\Omega \\ &= \frac{1}{2\pi}\int_{-\infty}^{\infty}U(\Omega)e^{i\Phi(\Omega)}e^{i\Omega t}\mathrm{d}\Omega \end{aligned} \quad (1)$$

where Ω_0 is the central frequency, $I(t)$ is the temporal intensity profile and $\phi(t)$ is the temporal phase including attosecond chirps. $U(\Omega)$ and $\Phi(\Omega)$ are the spectral amplitude and phase respectively. The XUV photon energy Ω is assumed to be much greater than the ionization threshold $I_p = 15.76$ eV so that the electron wave-packet created by XUV lies in the continuum regime. The kinetic energy of the photoelectron is $E = \Omega - I_p$. The IR field is assumed to be monochromatic such as

$$\tilde{E}_L = \frac{E_{IR}}{2}e^{i\omega\tau} \quad (2)$$

where ω is the IR photon energy. For a typical 800 nm laser $\omega = 1.55$ eV. τ represents the time delay between the XUV and IR fields. We only consider photoelectrons ionized from the outer shell of the argon atom so that single active electron approximation (SAE) can be applied. The effective potential of the ionic core is modeled by

$$V(r) = -\frac{Z + a_1e^{-a_2r} + a_3re^{-a_4r} + a_5e^{-a_6r}}{r}. \quad (3)$$

where Z=1 is the asymptotic charge seen by the active electron. The coefficients a_i are obtained by fitting the numerical potential calculated from the self-interaction free density functional theory, which can be found in Ref.[53] for argon atom. The ground state of argon has angular quantum number $l_i = 1$ and magnetic quantum number $m_i = 0, \pm 1$.

We consider ionization from $m_i = 0$ state only for linearly polarized light along z-axis. The detected photoelectron has a momentum $\mathbf{k} = (\sqrt{2E}, \theta, \varphi)$ where θ and φ are angles of detection with respect to the z-axis. Due to azimuthal symmetry the photoelectron spectrum is independent of φ. When both XUV and IR fields are weak the spectrogram $S(E, \theta, \tau)$ can be modeled by perturbation theory

$$\begin{aligned} S(E,\theta,\tau) &= \Big|\tilde{E}^*_{XUV}(\Omega)d_d(E,\theta) \\ &\quad +\tilde{E}^*_{XUV}(\Omega-\omega)\frac{E_{IR}}{2}e^{-i\omega\tau}d_a(E,\theta) \\ &\quad +\tilde{E}^*_{XUV}(\Omega+\omega)\frac{E_{IR}}{2}e^{i\omega\tau}d_e(E,\theta) \\ &\quad +o(E^2_{IR})\Big|^2 \end{aligned} \quad (4)$$

The first term in Eq.(4) describes the process that the electron initially at ground state absorbs one XUV photon Ω and transits to continuum state with energy E. d_d denotes the one-photon dipole transition matrix element. The second term in Eq.(4) corresponds to the path that the electron first absorbs one XUV photon $\Omega - \omega$ and then absorbs one IR photon ω, while the third term corresponds to the path that the electron first absorbs one XUV photon $\Omega + \omega$ and then emits one IR photon ω. d_a and d_e denote the two-photon transition matrix elements for the absorption and emission path respectively. The complex conjugate in Eq.(4) is consistent with our definition of Fourier transform in Eq.(1). The term $o(E^2_{IR})$ includes contributions from higher order paths involving two or more IR photons. The total spectrogram is the modulus square of the coherent superposition of all possible quantum paths that lead to a final state with energy E. Since $\omega \ll I_p$ for noble gas atoms, contribution from the path that the electron first absorbs (or emits) one IR photon and then one XUV photon is negligible[54]. Therefore in the present work we only include paths that the electron absorbs one XUV photon first.

We can expand $S(E, \theta, \tau)$ by the order of E_{IR},

$$S(E,\theta,\tau) = S_{XUV}(E,\theta) + S_{FSI}(E,\theta,\tau) + o(E^2_{IR}). \quad (5)$$

Here $S_{XUV}(E,\theta) = |U(\Omega)|^2|d_d(E,\theta)|^2$ is the IR free XUV–only photoelectron spectrum. $S_{FSI}(E,\theta,\tau)$ comes from the interference between one photon and two photon paths, which is proportional to E_{IR}

$$\begin{aligned} S_{FSI} &= E_{IR}\mathrm{Re}\{\tilde{E}^*_{XUV}(\Omega)\tilde{E}_{XUV}(\Omega-\omega)e^{i\omega\tau}d_d d^*_a \\ &\quad +\tilde{E}^*_{XUV}(\Omega)\tilde{E}_{XUV}(\Omega+\omega)e^{-i\omega\tau}d_d d^*_e\} \\ &= E_{IR}U(\Omega)|d_d|\{U(\Omega-\omega)|d_a|\cos(\omega\tau+\Delta_a) \\ &\quad +U(\Omega+\omega)|d_e|\cos(\omega\tau+\Delta_e)\} \quad (6) \\ &= A(E,\theta)\cos(\omega\tau+\Psi(E,\theta)) \quad (7) \end{aligned}$$

Eq.(6) implies that the FSI term is a superposition of two oscillating terms: one comes from the interference between the direct and the absorption path (d-a interference), the other comes from the interference between

the direct and the emission path (d-e interference). For a given (E,θ) the FSI term oscillates with τ at the IR frequency ω, as shown by Eq.(7). A and Ψ are the amplitude and phase of such oscillation given by

$$\begin{aligned} A &= E_{IR}U(\Omega)|d_d|\{|U(\Omega-\omega)|^2|d_a|^2+|U(\Omega+\omega)|^2|d_e|^2 \\ &\quad +2U(\Omega-\omega)U(\Omega+\omega)|d_a||d_e|\cos(\Delta_a-\Delta_e)\}^{\frac{1}{2}} \quad (8) \end{aligned}$$

$$\Psi = \tan^{-1}\left(\frac{U(\Omega-\omega)|d_a|\sin\Delta_a+U(\Omega+\omega)|d_e|\sin\Delta_e}{U(\Omega-\omega)|d_a|\cos\Delta_a+U(\Omega+\omega)|d_e|\cos\Delta_e}\right) \quad (9)$$

The phase Δ_a or Δ_e depends on the spectral phase $\Phi(\Omega)$ and the phase of dipole matrix elements

$$\Delta_a = \Phi(\Omega-\omega)-\Phi(\Omega)+\arg(d_d)-\arg(d_a) \quad (10)$$

$$\Delta_e = \Phi(\Omega)-\Phi(\Omega+\omega)+\arg(d_e)-\arg(d_d) \quad (11)$$

Eqs.(8)–(11) are used to retrieve the spectral phase $\Phi(\Omega)$ assuming that the spectral amplitude $U(\Omega)$ is already known. Clearly adding a constant to $\Phi(\Omega)$ does not change Δ_a or Δ_e, thus the FSI term carries information of the relative phase only. Therefore characterization method that is based on the analysis of FSI can retrieve only the relative spectral phase which determines the temporal pulse shape and duration. Since the absolute spectral phase is not determined, the CEP of the XUV pulse in the time domain is not fixed in this method. On the other hand, Liu *et al.*[55] have demonstrated that the photoelectron spectra generated by a single attosecond pulse in the presence of an intense IR field ($4.5\times10^{13}\mathrm{W/cm^2}$) are sensitive to the CEP of the attosecond pulse. This CEP dependence can be understood in terms of the coherent superposition of two electron wave packets. The electron in the first wave packet comes from direct photoionization by absorbing one XUV photon, while the electron in the second wave packet is released by the intense IR field and then rescatters on the parent ion. This method requires intense IR pulse where strong field ionization theory is usually less accurate.

In practice, one cannot decompose the perturbation series from an experimental spectrogram $S(E,\theta,\tau)$ directly. However, one can apply the Fourier decomposition with respect to τ such that

$$S(E,\theta,\tau) = S_0(E,\theta)+S_\omega(E,\theta,\tau)+S_{2\omega}(E,\theta,\tau)+\ldots. \quad (12)$$

Here $S_0 = S_{XUV}+o(E_{IR}^2)$ is a d.c. term that is independent of τ, $S_\omega = S_{FSI}+o(E_{IR}^3)$ oscillates with τ at a frequency ω, and $S_{2\omega}=o(E_{IR}^2)$ oscillates with τ at a frequency 2ω. When the IR intensity is weak, $S_0\approx S_{XUV}$, $S_\omega\approx S_{FSI}$, and $S_{2\omega}$ is negligible. Thus the FSI term is obtained by applying a filter on the measured spectrogram and then selecting its omega component. Note that in the case of single attosecond pulse, $S_{2\omega}$ is due to the interference not only between the two two-photon paths as in the RABBIT case, but also between the one-photon path and the three photon path (absorbing or emitting two IR photons). In either case there is a contribution proportional to E_{IR}^2.

B. One- and two-photon dipole transition matrix elements

In order to characterize the XUV pulse, complex matrix elements d_d, d_a, d_e in Eq.(4) are required. We consider the field free Hamiltonian

$$H_0 = -\frac{1}{2}\nabla^2+V(r) \quad (13)$$

The eigenstates of H_0 consists of both bound and continuum part. The ground state of argon atom can be written as

$$\langle\mathbf{r}|i\rangle = \frac{u_i(r)}{r}Y_{10}(\theta_r,\varphi_r) \quad (14)$$

where $\mathbf{r}=(r,\theta_r,\varphi_r)$ is the position vector and Y_{lm} is a spherical harmonic. The continuum state with energy $E=k^2/2$ and quantum numbers l, m are given as

$$\langle\mathbf{r}|klm\rangle = \frac{u_{kl}(r)}{r}Y_{lm}(\theta_r,\varphi_r) \quad (15)$$

The energy normalized radial wave function $u_{kl}(r)$ has the asymptotic form

$$\lim_{r\to\infty}u_{kl}(r) = \sqrt{\frac{2}{\pi k}}\sin\left(kr+\frac{Z}{k}\ln(2kr)+\eta_l(E)\right) \quad (16)$$

$$\eta_l(E) = -\frac{l\pi}{2}+\sigma_l(E)+\delta_l(E) \quad (17)$$

where $\sigma_l=\arg[\Gamma(l+1-iZ/k)]$ is the Coulomb phase shift, δ_l is the partial wave phase shift due to the short range deviation from a pure Coulomb potential.

The final photoelectron state with momentum $\mathbf{k}=(\sqrt{2E},\theta,\varphi)$ can be expanded by partial waves

$$\langle\mathbf{r}|\mathbf{k}^{(-)}\rangle = \sum_{L,M}e^{-i\eta_L(E)}Y_{LM}^*(\theta,\varphi)Y_{LM}(\theta_r,\varphi_r)\frac{u_{kL}(r)}{r} \quad (18)$$

This wavefunction behaves asymptotically as the superposition of a plane wave plus an incoming spherical wave.

Since $z=r\cos\theta_r$, the one-photon dipole transition matrix element can be calculated as the following

$$\begin{aligned} d_d(E,\theta) &= \langle\mathbf{k}^{(-)}|z|i\rangle \\ &= \sum_{L,M}e^{i\eta_L(E)}Y_{LM}(\theta,\varphi)\langle Y_{LM}|\cos\theta_r|Y_{10}\rangle\langle u_{kL}|r|u_i\rangle \\ &= \sqrt{\frac{1}{12\pi}}\{P_0(\cos\theta)e^{i\eta_0(E)}\langle u_{k0}|r|u_i\rangle \\ &\quad +2P_2(\cos\theta)e^{i\eta_2(E)}\langle u_{k2}|r|u_i\rangle\} \quad (19) \end{aligned}$$

From Eq.(19) d_d consists of s wave and d wave so that d_d is symmetric with respect to the polarization axis.

The two-photon transition matrix element is given as

$$\begin{aligned} d_\kappa(E,\theta) &= \lim_{\epsilon\to 0}\sum_{\alpha,\lambda,m}\frac{\langle \mathbf{k}^{(-)}|z|\alpha\lambda m\rangle\langle\alpha\lambda m|z|i\rangle}{E_\kappa - E_\alpha + i\epsilon} \\ &= \sum_{L,M,\lambda,m} e^{i\eta_L(E)}Y_{LM}(\theta,\varphi)\langle Y_{LM}|\cos\theta_r|Y_{\lambda m}\rangle \\ &\quad\times\langle Y_{\lambda m}|\cos\theta_r|Y_{10}\rangle W_{L,\lambda}(E,E_\kappa) \\ &= \sqrt{\frac{1}{12\pi}}\{P_1(\cos\theta)e^{i\eta_1(E)}W_{1,0}(E,E_\kappa) \\ &\quad+\frac{4}{5}P_1(\cos\theta)e^{i\eta_1(E)}W_{1,2}(E,E_\kappa) \\ &\quad+\frac{6}{5}P_3(\cos\theta)e^{i\eta_3(E)}W_{3,2}(E,E_\kappa)\} \end{aligned} \tag{20}$$

The label κ can be replaced by either a (absorbing one IR photon, $E_a = E-\omega$) or e (emitting one IR photon, $E_e = E+\omega$). In Eq.(20) we introduce a two-photon radial matrix element reads

$$W_{L,\lambda}(E,E_\kappa) = \lim_{\epsilon\to 0}\sum_\alpha \frac{\langle u_{kL}|r|u_{\alpha\lambda}\rangle\langle u_{\alpha\lambda}|r|u_i\rangle}{E_\kappa - E_\alpha + i\epsilon} \tag{21}$$

$W_{L,\lambda}(E,E_\kappa)$ is a summation over all intermediate states with energy E_α, including both bound and continuum, while the angular quantum numbers are fixed. From Eq.(20) d_a and d_e consist of p wave and f wave so that they are antisymmetric with respect to the polarization axis. Furthermore, we can see that $S_{XUV}(E,\theta)$ is symmetric and $S_{FSI}(E,\theta,\tau)$ is antisymmetric with respect to the polarization axis.

C. Dalgarno-Lewis method for calculating two-photon matrix elements

The radial wave function $u_{\alpha\lambda}(r)$ is the eigenfunction of the radial Hamiltonian

$$H_\lambda = -\frac{1}{2}\frac{\partial^2}{\partial r^2} + V(r) + \frac{\lambda(\lambda+1)}{2r^2} \tag{22}$$

with the eigenvalue E_α. The radial matrix element $W_{L,\lambda}(E,E_\kappa)$ can be rewritten by introducing the resolvent operator

$$\begin{aligned} W_{L,\lambda}(E,E_\kappa) &= \langle u_{kL}|r(\lim_{\epsilon\to 0}\frac{1}{E_\kappa - H_\lambda + i\epsilon})r|u_i\rangle \\ &= \langle u_{kL}|r|\rho_{\kappa\lambda}\rangle \end{aligned} \tag{23}$$

The intermediate radial wave function

$$\begin{aligned} \rho_{\kappa\lambda}(r) &= (\lim_{\epsilon\to 0}\frac{1}{E_\kappa - H_\lambda + i\epsilon})r|u_i\rangle \\ &= (\wp\frac{1}{E_\kappa - H_\lambda} - i\pi\delta(E_\kappa - H_\lambda))r|u_i\rangle \\ &= \rho^{(R)}_{\kappa\lambda} - i\pi u_{\kappa\lambda}\langle u_{\kappa\lambda}|r|u_i\rangle \end{aligned} \tag{24}$$

Here $\wp$ prescribes the principal value integration that contributes to the real part of $\rho_{\kappa\lambda}$ (off-shell part). δ represents the Dirac delta function that contributes to the imaginary part of $\rho_{\kappa\lambda}$ (on-shell part). The real wave function $\rho^{(R)}_{\kappa\lambda}(r)$ is the solution of the following inhomogeneous ordinary differential equation

$$(E_\kappa - H_\lambda)\rho^{(R)}_{\kappa\lambda}(r) = ru_i(r) \tag{25}$$

with the boundary condition $\rho^{(R)}_{\kappa\lambda}(r) = 0$ at $r = 0$. This approach of calculating $W_{L,\lambda}$ is known as the Dalgarno-Lewis method [52].

In our problem $E_\kappa = \kappa^2/2$ is a positive energy, so that $\rho_{\kappa\lambda}(r)$ is required to be a continuum wave function which behaves as a complex outgoing wave asymptotically[56].

$$\lim_{r\to\infty}\rho_{\kappa\lambda}(r) = -\pi\sqrt{\frac{2}{\pi\kappa}}e^{i\left(\kappa r + \frac{Z}{\kappa}\ln(2\kappa r) + \eta_\lambda(E_\kappa)\right)}\langle u_{\kappa\lambda}|r|u_i\rangle \tag{26}$$

In order to fulfill the asymptotic form Eq.(26), the physical solution of Eq.(25) should have the smallest asymptotic amplitude as discussed in Ref. [57].

Instead of solving the Dalgarno-Lewis equation [Eq.(25)], for simplicity if one substitutes the asymptotic form of $u_{kL}(r)$ and $\rho_{\kappa\lambda}(r)$ into Eq.(23), one would obtain an approximate result[50, 51]

$$W_{L,\lambda}(E,E_\kappa) \approx ie^{i\{\eta_\lambda(E_\kappa)-\eta_L(E)\}}\langle u_{\kappa\lambda}|r|u_i\rangle T^{cc}(E,E_\kappa) \tag{27}$$

Here $\langle u_{\kappa\lambda}|r|u_i\rangle$ is the radial part of the one-photon transition matrix element from the ground state to an intermediate continuum state. The term T^{cc} accounts for the continuum-continuum transition and has an analytical form:

$$\begin{aligned} T^{cc}(E,E_\kappa) &= -\frac{1}{\sqrt{k\kappa}}\frac{(2\kappa)^{iZ/\kappa}}{(2k)^{iZ/k}}\left(\frac{i}{\kappa-k}\right)^{2+i(Z/\kappa - Z/k)} \\ &\quad\times\Gamma[2+i(Z/\kappa - Z/k)] \end{aligned} \tag{28}$$

D. Approximations in atomic parameters by the PROOF and iPROOF methods

According to the discussion in Sec.II.A, the spectrogram measured along a particular direction is sufficient to retrieve the spectral phase. To simplify our analysis, in the following discussion we focus on photoelectrons detected along the $+z$ direction. Thus $\theta = 0$ and $P_L(\cos\theta) = 1$. Therefore

$$d_d(E) = \sqrt{\frac{1}{12\pi}}\{e^{i\eta_0(E)}\langle u_{k0}|r|u_i\rangle + 2e^{i\eta_2(E)}\langle u_{k2}|r|u_i\rangle\} \tag{29}$$

$$\begin{aligned} d_\kappa(E) &= \sqrt{\frac{1}{12\pi}}\{e^{i\eta_1(E)}W_{1,0}(E,E_\kappa) + \frac{4}{5}e^{i\eta_1(E)} \\ &\quad\times W_{1,2}(E,E_\kappa) + \frac{6}{5}e^{i\eta_3(E)}W_{3,2}(E,E_\kappa)\} \end{aligned} \tag{30}$$

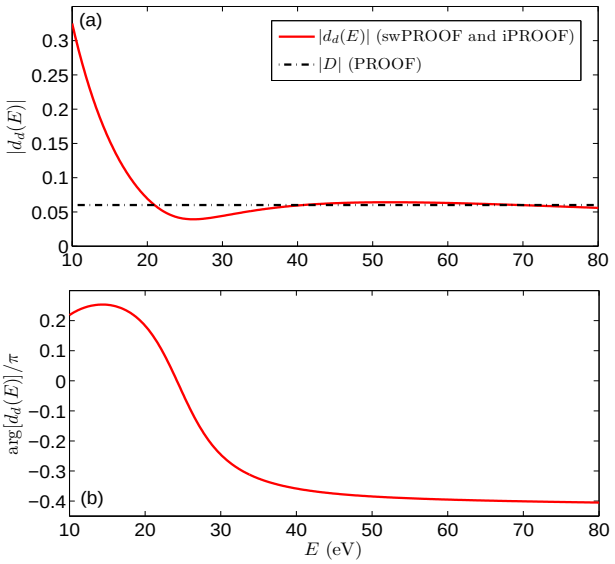

FIG. 1: (Color online) (a) Amplitude and (b) phase of the one-photon dipole transition matrix element $d_d(E)$ of argon.

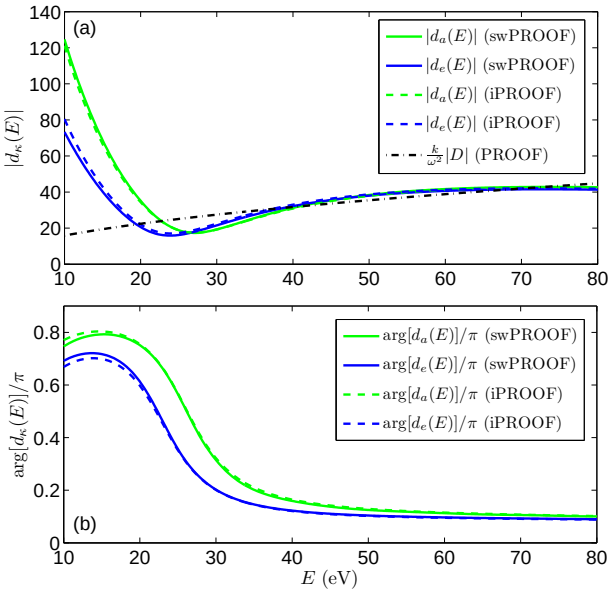

FIG. 2: (Color online) (a) Amplitude and (b) phase of the two-photon transition matrix element $d_a(E)$ (green or light gray) and $d_e(E)$ (blue or dark gray) of argon. For the swPROOF method (solid), the iPROOF method (dashed) and the PROOF method (dot-dashed line). ($\omega = 1.55$ eV)

In the swPROOF method we use the Dalgarno-Lewis approach to calculate accurate $d_\kappa(E)$. If $W_{L,\lambda}(E, E_\kappa)$ is replaced by its asymptotic approximation Eq.(27), $d_\kappa(E)$ is reduced to a simple form

$$d_\kappa(E) = iT^{cc}(E, E_\kappa)d_d(E_\kappa). \tag{31}$$

Eq.(31) is the basis of the iPROOF method[48]. In this approximation the two-photon matrix element can be explicitly separated into two terms — a single XUV photon dipole transition matrix element, times a continuum-continuum transition amplitude T^{cc} in the presence of an IR field. The amplitude and phase part can be written separately

$$|d_\kappa(E)| = T^{cc}_\kappa(E)|d_d(E_\kappa)| \tag{32}$$

$$\arg[d_\kappa(E)] = \arg[d_d(E_\kappa)] + \varphi^{cc}_\kappa(E) + \frac{\pi}{2} \tag{33}$$

where

$$T^{cc}_\kappa(E) = |T^{cc}(E, E_\kappa)| \tag{34}$$

$$\varphi^{cc}_\kappa(E) = \arg[T^{cc}(E, E_\kappa)] \tag{35}$$

are the amplitude and phase of the continuum-continuum term.

The one-photon transition matrix element d_d calculated by using the model potential Eq.(3) for argon are shown in FIG.1. $|d_d(E)|$ shows a minimum (Cooper minimum [58]) at $E = 26$ eV (corresponding $\Omega = 42$ eV), and the phase $\arg[d_d(E)]$ shows a significant jump around this minimum.

In FIG.2 two-photon transition matrix elements d_a and d_e are shown. $|d_a|$ and $|d_e|$ are two orders of magnitude larger than $|d_d|$, and the minima of $|d_a|$ and $|d_e|$ are relatively deeper. Note that the minima of $|d_a|$ and $|d_e|$ shift toward opposite directions. The phases of d_a and d_e also show rapid change near the minima. The discrepancy between the two-photon matrix elements in the swPROOF method and the iPROOF method mainly lies in the low energy region.

Further approximations can be introduced to derive the PROOF method[49]. First, we neglect the long-range Coulomb potential by setting $Z = 0$ in Eq.(28), which is consistent with the strong field approximation (SFA):

$$T^{cc}(E, E_\kappa) = \frac{1}{\sqrt{k\kappa}} \frac{1}{(\kappa - k)^2} \tag{36}$$

Furthermore, we assume $\omega \ll E$ which is often referred to as the soft-photon approximation[59, 60]:

$$E_\kappa = E \mp \omega \Rightarrow \kappa = k\sqrt{1 \mp \frac{2\omega}{k^2}} \approx k \mp \frac{\omega}{k} \tag{37}$$

$$T^{cc}(E, E_\kappa) \approx \frac{1}{\sqrt{k^2 \mp \omega}\left(\mp\frac{\omega}{k}\right)^2} \approx \frac{k}{\omega^2} \tag{38}$$

Thirdly, the atomic physics in photoionization process is also neglected. The bound-free transition matrix element reduces to a constant $d_d(E) \approx D$. Therefore

$$d_\kappa(E) = i\frac{k}{\omega^2}D \tag{39}$$

In this work we assign $|D| = 0.06$, the corresponding $|d_d(E)|$ and $|d_\kappa(E)|$ used in the PROOF method are plotted in black dot-dashed line in FIG.1 and FIG.2 respectively. FIG.3 shows the ratio $|d_a(E)|/|d_d(E-\omega)|$ and $|d_e(E)|/|d_d(E+\omega)|$ for the swPROOF, iPROOF and PROOF method. One can see that the PROOF method leads to large error in the low energy region, whereas for $k > 1.7$ a.u. or $E > 40$ eV these three methods match each other quite well.

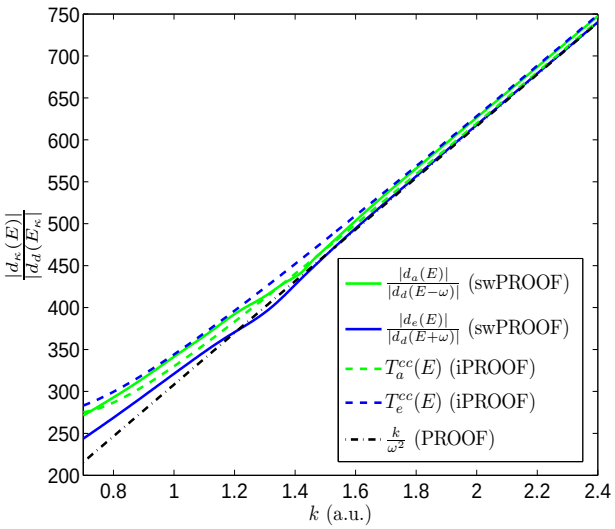

FIG. 3: (Color online) The ratio $|d_a(E)|/|d_d(E-\omega)|$ (green or light gray) and $|d_e(E)|/|d_d(E+\omega)|$ (blue or dark gray) for the swPROOF method (solid), the iPROOF method (dashed) and the PROOF method (dot-dashed line). ($\omega = 1.55$ eV)

One can also rewrite the phase Δ_a or Δ_e in Eqs.(10) and (11) by introducing an atomic phase ψ_a or ψ_e such that

$$\Delta_a(E) = \Phi(\Omega-\omega) - \Phi(\Omega) + \psi_a(E) - \frac{\pi}{2} \tag{40}$$

$$\Delta_e(E) = \Phi(\Omega) - \Phi(\Omega+\omega) + \psi_e(E) + \frac{\pi}{2} \tag{41}$$

The atomic phase ψ_a and ψ_e are in general given by

$$\psi_a(E) = \arg[d_d(E)] - \arg[d_a(E)] + \frac{\pi}{2} \tag{42}$$

$$\psi_e(E) = \arg[d_e(E)] - \arg[d_d(E)] - \frac{\pi}{2} \tag{43}$$

In the iPROOF method, according to Eq.(33)

$$\psi_a(E) = \arg[d_d(E)] - \arg[d_d(E-\omega)] - \varphi_a^{cc}(E) \tag{44}$$

$$\psi_e(E) = \arg[d_d(E+\omega)] - \arg[d_d(E)] + \varphi_e^{cc}(E) \tag{45}$$

In the PROOF method

$$\psi_a(E) = \psi_e(E) = 0 \tag{46}$$

FIG.4 shows the atomic phase $\psi_a(E)$ and $\psi_e(E)$ in the swPROOF and the iPROOF method. They are all negative and quite close to each other. Each atomic phase has a sharp valley around the Cooper minimum. For the energy region $E > 40$ eV, $|\psi_a(E)| \approx |\psi_e(E)| < 0.02\pi$ so it would be reasonable to remove the atomic phase as PROOF does. From Eqs.(40)(41) one can deduce that as long as ω is small and the spectral phase $\Phi(\Omega)$ changes smoothly over a broad frequency range, Δ_a and Δ_e are roughly differ by π. Thus the d-a interference and the d-e interference in Eq.(6) tend to be out of phase and the FSI term is actually a result of strong cancelation between these two oscillating terms. This makes it essential to calculate the atomic phases accurately.

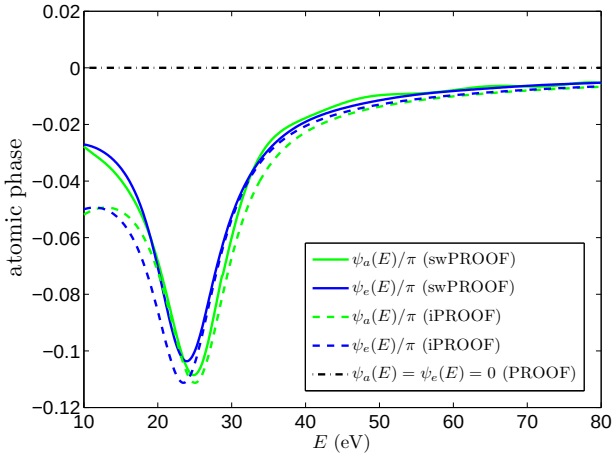

FIG. 4: (Color online) The atomic phase $\psi_a(E)$ (green or light gray) and $\psi_e(E)$ (blue or dark gray) in the swPROOF method (solid), the iPROOF method (dashed) and the PROOF method (dot-dashed line). ($\omega = 1.55$ eV)

E. Continuum-continuum time delay

The atomic phases given in Eq.(42) to Eq.(45) are important for many recent studies on attosecond time delays in photoionization experiments [18, 19, 22]. It is "believed" that these time delays can reveal some aspects of the electron dynamics. Since the time delay is measured in the presence of a dressing IR field, the effect of the IR field has to be accurately accounted for in order to extract effective information of the atomic target under the XUV alone. In an intense IR field, the standard strong field approximation (SFA) assumes that the photoelectron is driven by the IR field freely, which is not accurate enough to interpret the time delay in attosecond time scale. Under various approximations beyond SFA, it has been claimed that the interplay of the probe IR field and the long-range Coulomb potential (so-called Coulomb-laser coupling) leads to an additive time delay, so that the measured time delay can be separated into

an intrinsic Wigner-like delay[61, 62] and an IR-induced delay due to Coulomb-laser coupling[63, 64].

This separation can also be seen within the perturbation theory supposing the field is weak[19, 22]. From Eqs.(6),(40), and (41) one can define a time delay via either d-a interference or d-e interference:

$$\tau_a = \frac{\Delta_a}{\omega} = \frac{\Phi(\Omega-\omega)-\Phi(\Omega)}{\omega} + \frac{\psi_a}{\omega} - \frac{\pi}{2\omega} \tag{47}$$

$$\tau_e = \frac{\Delta_e}{\omega} = \frac{\Phi(\Omega)-\Phi(\Omega+\omega)}{\omega} + \frac{\psi_e}{\omega} + \frac{\pi}{2\omega} \tag{48}$$

On the righthand side of Eq.(47) or (48), the first term is the finite-difference approximation of $-\partial\Phi/\partial\Omega$ which is the group delay of the XUV field. The second term yields an atomic time delay $\tau_a^{at}(E) = \psi_a(E)/\omega$ or $\tau_e^{at}(E) = \psi_e(E)/\omega$. The atomic delay can be calculated from the one and two-photon transition matrix element via Eqs.(42),(43) in general. When the asymptotic approximation is applied as in the iPROOF method, see Eqs.(44) and (45), the atomic delay can be separated into two parts explicitly:

$$\tau_a^{at}(E) = \tau_a^{W}(E) + \tau_a^{cc}(E) \tag{49}$$

$$\tau_e^{at}(E) = \tau_e^{W}(E) + \tau_e^{cc}(E) \tag{50}$$

The first part

$$\tau_a^{W}(E) = \frac{\arg[d_d(E)] - \arg[d_d(E-\omega)]}{\omega} \tag{51}$$

$$\tau_e^{W}(E) = \frac{\arg[d_d(E+\omega)] - \arg[d_d(E)]}{\omega} \tag{52}$$

is the finite-difference approximation of $\partial\{\arg d_d\}/\partial E$, which is a Wigner-like delay in single-photon ionization. This delay is related to the electron dynamics following the absorption of an XUV photon. The second part is a continuum-continuum delay induced by the IR transition taking into account the long-range potential with a Coulomb tail, given by $\tau_a^{cc}(E) = -\varphi_a^{cc}(E)/\omega$ or $\tau_e^{cc}(E) = \varphi_e^{cc}(E)/\omega$. The continuum-continuum phase φ_κ^{cc} is obtained via Eqs.(28) and (35). Beyond the asymptotic approximation used in iPROOF, one can also correct the long-range amplitude of the asymptotic wavefunction $u_{kL}(r)$ and $\rho_{\kappa\lambda}(r)$ so that the continuum-continuum phase can be corrected by an additional term[51]:

$$\tilde{\varphi}_\kappa^{cc} = \varphi_\kappa^{cc} + \arg\left[1 + \frac{iZ}{2}\left(\frac{1}{\kappa^2}+\frac{1}{k^2}\right)\frac{\kappa-k}{1+iZ(1/\kappa-1/k)}\right] \tag{53}$$

FIG.5 (a) shows the Wigner-like delay τ^W, see Eqs. (51) and (52). τ_a^W and τ_e^W are not identical since they are finite difference to the left side and to the right side respectively. In the low energy region where the variation of the dipole phase in an energy scale comparable or less than the difference step $\omega = 1.55$ eV, the finite difference to the left and to the right side have considerable discrepancy. From this figure the Wigner-like delay in general is negative and has a minimum of -110 as roughly near the Cooper minimum.

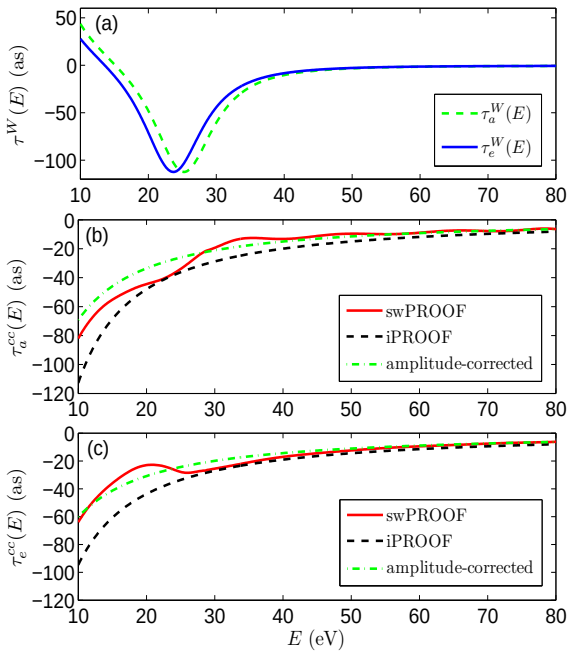

FIG. 5: (Color online) (a) the Wigner-like delay calculated from the one-photon dipole transition matrix element. (b) τ_a^{cc} obtained from the asymptotic approximation used in iPROOF (dashed) and from the long-range amplitude-corrected asymptotic approximation (dot-dashed), compared with the corresponding value that was obtained via subtracting the Wigner-like delay from the atomic delay given in swPROOF method (solid). (c) same as (b) but for τ_e^{cc}. ($\omega = 1.55$ eV)

In FIG.5 (b) and (c) we plot the continuum-continuum delay τ^{cc} calculated analytically from the asymptotic approximation (iPROOF) and the long-range amplitude-corrected asymptotic approximation Eq.(53). In order to check the validity of the separation of the atomic delay into two additive parts mentioned above, we also plot the "effective" continuum-continuum delay extracted from the accurate matrix element (as used in swPROOF method). This value is obtained by subtracting the Wigner-like delay from the atomic delay calculated via Eqs.(42),(43) directly. One can see that in the high energy limit the amplitude-corrected asymptotic approximation tends to reproduce the swPROOF result, whereas the asymptotic approximation (iPROOF) yields a relatively larger delay in magnitude. In the low energy region, the separation of atomic time delay is not very accurate. Thus when utilizing the analytical continuum-continuum delay to extract a Wigner-like time delay from the atomic time delay, the error may become tens of attosecond in magnitude. At a first glance our result looks

quite opposite to the result in Ref.[65, 66] where the separation of atomic time delay is verified, however they are actually consistent. Note that Ref.[65, 66] utilizes a RABITT-type experiment so that the atomic time delay is defined through a-e interference. The Wigner-like delay, continuum-continuum delay and atomic delay in Ref.[65, 66] correspond to the average of d-a and d-e values in our calculation. When averaging Fig.5 (b) and (c), one can expect that the difference between swPROOF and amplitude-corrected data will be greatly reduced, which is in agreement with Ref.[65, 66]. We comment that the verification in Ref.[65, 66] is actually an average effect which may not be successful for all targets and for all energy regions.

III. RESULTS AND DISCUSSION

A. Comparison of FSI terms between TDSE and theoretical models

We simulate the XUV+IR spectra for argon by solving the single active electron TDSE numerically. The model potential for argon is given in Eq.(3). The discrete variable representation (DVR) basis set is used in the computation. Details of the numerical method has been represented in Ref.[67, 68]. An 800 nm IR pulse with peak intensity 10^{11} W/cm^2 is used in this simulation which mimics the typical experimental condition. To reduce the computational load we limit ourselves to a relative short IR pulse (8.8 fs in FWHM) with a cosine-squared envelope. The box size and number of grid points were chosen to ensure convergence. The XUV pulses have the same pre-determined spectral amplitude $U(\Omega)$ but several different spectral phases $\Phi(\Omega)$ are chosen.

FIG.6(a) shows a Gaussian amplitude with central frequency at 60 eV and bandwidth of 22 eV, which would correspond to a FWHM duration of 83 as for a transform-limited pulse. The four input spectral phases and the zoomed-in phases near the central frequency are plotted in FIG.6(b) and (c) respectively. We always set $\Phi(\Omega) = 0$ at the central frequency – recall that the absolute phase cannot be retrieved. FIG.6(d) shows the intensity profile in the time domain for each pulse, indicating that the duration ranges from 87 to 235 as, while peak intensity from 9.0 – 3.0 $\times 10^{11}$ W/cm^2, also the peak position can shift by 100 as for different pulses.

FIG.7 (a) shows the spectrogram obtained from TDSE simulation for electrons detected along the +z direction and for the XUV pulse case 2 in FIG.6. FIG.7(b) shows the magnitude of the Fourier components filtered from the spectrogram. Clearly the d.c. component S_0 is almost identical to the IR free spectra S_{XUV}, i.e., for XUV alone. This part is independent of the XUV phase. Our interest lies in the ω-component S_ω which can be treated as the FSI term. This part varies as the XUV phase changes, however it is about one order of magnitude smaller than the d.c. part. The 2ω-component $S_{2\omega}$ is

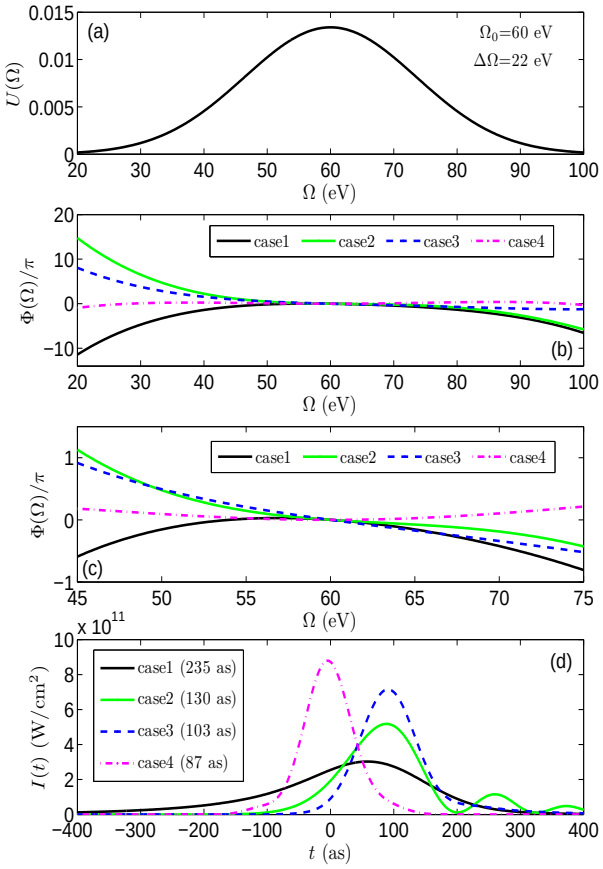

FIG. 6: (Color online) (a) The spectral amplitude (b) the whole spectral phase (c) the spectral phase zoomed in near the central frequency (d) the intensity profile in the time domain of four XUV pulses used in the simulation.

one more order smaller than the FSI term.

The FSI amplitude $A(E)$ and phase $\Psi(E)$ (see Eq.(7)) can be either extracted from the TDSE spectrogram or calculated from the known $U(\Omega)$, $\Phi(\Omega)$ and relevant matrix elements in the PROOF, iPROOF and swPROOF methods via Eqs.(8)–(11). FIG.8 shows the comparison of such results. $A(E)$ shows a valley and $\Psi(E)$ shows a large phase jump around the central energy $E_0 = \Omega_0 - I_p \approx 44$ eV. The overall agreement in $\Psi(E)$ is better than in $A(E)$, and the TDSE result is well reproduced by the swPROOF method where the atomic matrix elements are calculated using the Dalgarno-Lewis method. The remaining discrepancies between swPROOF and TDSE might result from the finite duration of the IR pulse used in the TDSE simulation, as opposed to a monochromatic wave assumed in the theoretical model. Although the difference in the individual matrix elements obtained in the swPROOF method and the iPROOF method is not significant (see FIG.2), $A(E)$ given by the iPROOF method shows considerable error. Remember the FSI term is the superposition of the d-a interference term and the d-e interference term as shown in Eq.(6). Since there is a strong cancelation between these two terms as we dis-

cussed at the end of Sec.II.D, the error in the final FSI term can become considerable even if the error in each individual interference term is small. The PROOF method yields even larger error in the low energy region. One can also see that $A(E)\cos\Psi(E)$ is roughly one fifth of $A(E)\sin\Psi(E)$ in magnitude.

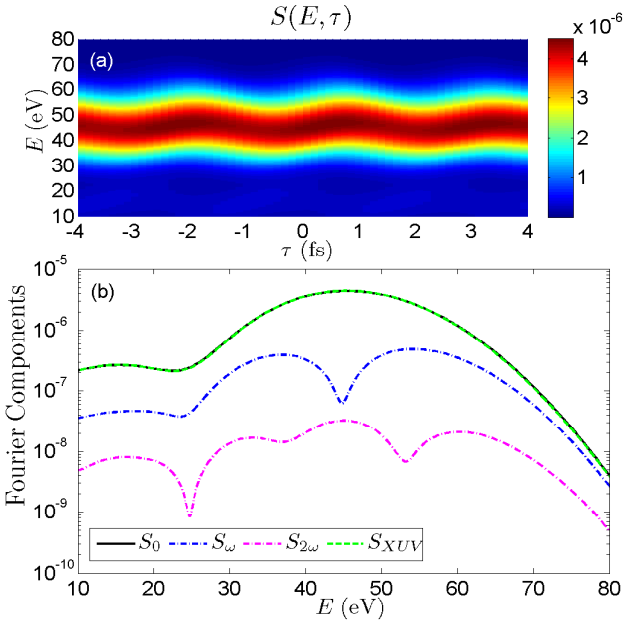

FIG. 7: (Color online) (a) TDSE simulated spectrogram for the electron detected along the $+z$ direction. The XUV pulse is chosen as case2 in FIG.6. The IR pulse has the following parameters: wavelength=800 nm, peak intensity=10^{11} W/cm^2, FWHM duration=8.8 fs, CEP=0, cosine-squared envelope. A positive τ means the IR pulse comes first. (b) Magnitude of the Fourier component S_0 (top solid), S_ω (middle dot-dashed) and $S_{2\omega}$ (bottom dot-dashed) filtered from (a), the TDSE result of the IR-free spectra S_{XUV} (top dashed line) is also plotted.

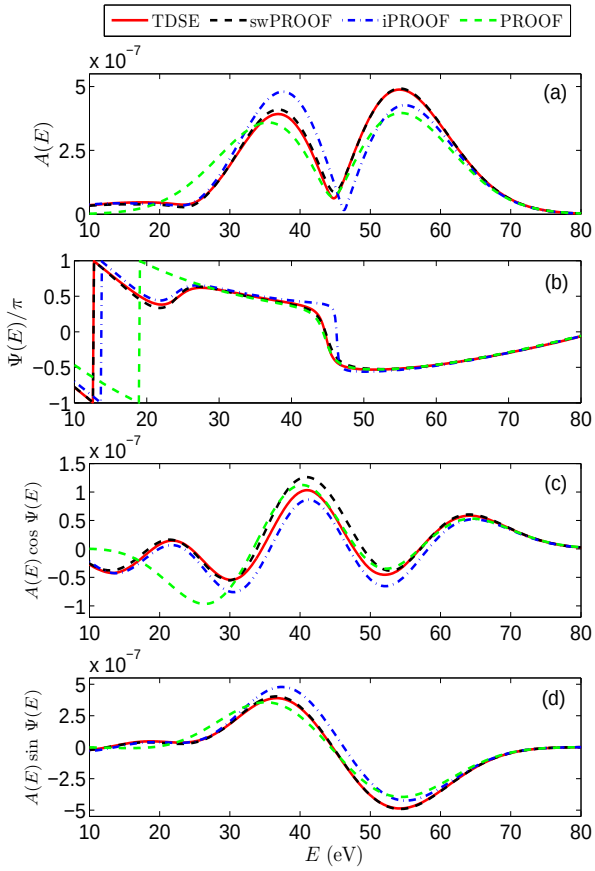

FIG. 8: (Color online) (a) $A(E)$ (b) $\Psi(E)$ (c) $A(E)\cos\Psi(E)$ (d) $A(E)\sin\Psi(E)$ extracted from the TDSE simulation FIG.7 (red solid) and calculated from the actual XUV pulse (case 2 in FIG.6) and the atomic matrix element in swPROOF (black or dark gray dashed), iPROOF (blue or dark gray dot-dashed) and PROOF(green or light gray dashed). Note that $A(E)$ and $\Psi(E)$ are not affected by the CEP of the XUV pulse.

FIG.9 presents the sensitivity of the FSI modulation as the spectral phase is varied. $A(E)$ is very insensitive to the spectral phase $\Phi(\Omega)$. Although $\Psi(E)$ is sensitive, its origin as the $\tan^{-1}$ function usually results in some discontinuity so it is more difficult to fit. As can be seen from FIG.9(c), $A(E)\cos\Psi(E)$ is not only sensitive to the spectral phase but also a smooth function of electron energy. Thus $A(E)\cos\Psi(E)$ is more suitable for fitting, as we shall show in the next subsection.

B. Accuracy of spectral phase retrieval

Starting from the simulated FSI modulation $A_{TDSE}(E)$, $\Psi_{TDSE}(E)$, the known spectral amplitude $U(\Omega)$, and the matrix element d_d, d_a, d_e in either swPROOF, iPROOF or PROOF method, one can retrieve the spectral phase $\Phi(\Omega)$ through the fitting procedure. We parameterize $\Phi(\Omega)$ as

$$\Phi_{guess}(\Omega) = \sum_{n=1}^{4} a_n(\Omega-\Omega_0)^n \qquad (54)$$

This implies the spectra phase is always set to zero at $\Omega_0 = 60$ eV which removes the arbitrariness of the constant phase. From Φ_{guess} one can calculate A_{guess}, Ψ_{guess} via Eqs.(8)–(11), and the optimal spectral phase Φ_{fit} is the one which minimizes an error function Q.

Two methods of spectral phase retrieval will be addressed here. First, we assume that the IR intensity (and thus E_{IR}) is known. This is to check the intrinsic accuracy of the three theoretical methods based on the modulation of the FSI term in the spectrogram. In this case, the error function is defined as

$$Q = \int_{10\text{eV}}^{80\text{eV}} [A_{TDSE}(E)\cos\Psi_{TDSE}(E) - A_{guess}(E)\cos\Psi_{guess}(E)]^2 \mathrm{d}E \qquad (55)$$

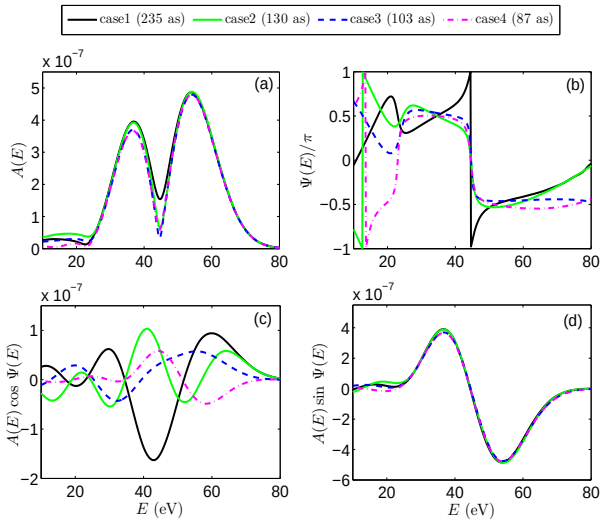

FIG. 9: (Color online) (a) $A(E)$ (b) $\Psi(E)$ (c) $A(E)\cos\Psi(E)$ (d) $A(E)\sin\Psi(E)$ extracted from TDSE simulation for four XUV pulses shown in FIG.6. The IR parameters are the same as in FIG.7.

Second, in experiments the IR intensity is generally not precisely determined, thus E_{IR} may be treated as another fitting parameter. Due to this additional uncertainty the error function has to include both $A(E)\cos\Psi(E)$ and $A(E)\sin\Psi(E)$ such as

$$\begin{aligned} Q = \int_{10\text{eV}}^{80\text{eV}} \{&[A_{TDSE}(E)\cos\Psi_{TDSE}(E) \\ &-A_{guess}(E)\cos\Psi_{guess}(E)]^2 \\ &+[A_{TDSE}(E)\sin\Psi_{TDSE}(E) \\ &-A_{guess}(E)\sin\Psi_{guess}(E)]^2\}\mathrm{d}E \end{aligned} \quad (56)$$

The optimization is done via a genetic algorithm (GA). We actually use the micro-GA which evolves small population including ten individuals[69, 70].

The comparison between the actual pulse and the retrieved pulse for case1 to case4 are shown in FIGs.10,11 and 12. The IR intensity used in TDSE simulation is $10^{11}\,\mathrm{W/cm^2}$ and this intensity is assumed to be known in the pulse retrieval. Note that pulses retrieved from different methods originally have different peak intensities as well as different peak positions in the time domain. However a streaking-type pulse characterization experiment is usually not expected to retrieve such parameters. To compare pulse shapes easily we have normalized (rescaled and shifted) each pulse such that its peak value is one and this peak appears at time zero. In FIGs.10 and 11 we also plot the comparison of the actual and retrieved spectral phase for case1 and case2. Clearly the spectral phase is well retrieved by the swPROOF method, the iPROOF has more error and the PROOF is even worse. The whole spectral phase retrieved by PROOF looks flatter than others, but it does not guarantee a transform limited pulse due to its non-zero curvature, see the zoom-in plot of the spectral phase. In TABLE I we list the pulse duration and peak position of the actual and retrieved XUV pulse from case1 to case4, respectively.

For case1, the pulse duration of the input pulse is 235 as which is to be compared to 83 as in the transform limited one. The pulse shape retrieved from swPROOF is the closest to the actual one, and the pulse duration extracted from swPROOF lies within better than 10% of the actual value. For iPROOF and PROOF, the errors become larger in general, especially that PROOF yields a quite different pulse shape. Additionally we notice that peak positions obtained from iPROOF and PROOF can easily differ by more than 20 as. For case2, the input pulse has duration of 130 as which is closer to 83 as. The pulse retrieved by swPROOF are in very good agreement with the input pulse. While in this case pulse durations retrieved from iPROOF and PROOF are acceptable, these two methods give different tail shapes from the input, and peak positions still shift by 12 as or more. For case3, the input pulse has duration of 103 as which can only be accurately reproduced by swPROOF. The iPROOF overestimates the pulse duration by more than 20% and the PROOF yields a transform-limited pulse. For case4, the input pulse has duration of 87 as which is very near the transform limited duration. All of these three methods can retrieve the pulse duration accurately, however the peak position given by iPROOF and PROOF still have errors more than 10 as.

These results provide the benchmark on how accurately the spectral phase or $E_{XUV}(t)$ of an isolated attosecond pulse can be determined in a given experiment even for such a highly idealized "experimental" situation. In our simulation even the swPROOF method may not exactly reproduce the actual XUV pulse. This error mainly results from the short IR pulse used in the simulation, and we believe that this error can be reduced if a longer IR pulse (for example over 20 fs) is used.

case1	Actual	swPROOF	iPROOF	PROOF
XUV pulse duration (as)	235	255	213	294
XUV peak position (as)	59	62	79	27
case2	Actual	swPROOF	iPROOF	PROOF
XUV pulse duration (as)	130	130	124	122
XUV peak position (as)	89	92	77	75
case3	Actual	swPROOF	iPROOF	PROOF
XUV pulse duration (as)	103	100	125	83
XUV peak position (as)	91	103	73	57
case4	Actual	swPROOF	iPROOF	PROOF
XUV pulse duration (as)	87	87	89	87
XUV peak position (as)	-4	-8	-14	-37

TABLE I: The actual and retrieved XUV pulse parameters for case 1–4 (read from FIG.10–12). The IR pulse used in the TDSE simulation has a peak intensity of $10^{11}\,\mathrm{W/cm^2}$. In the fitting procedure E_{IR} is known.

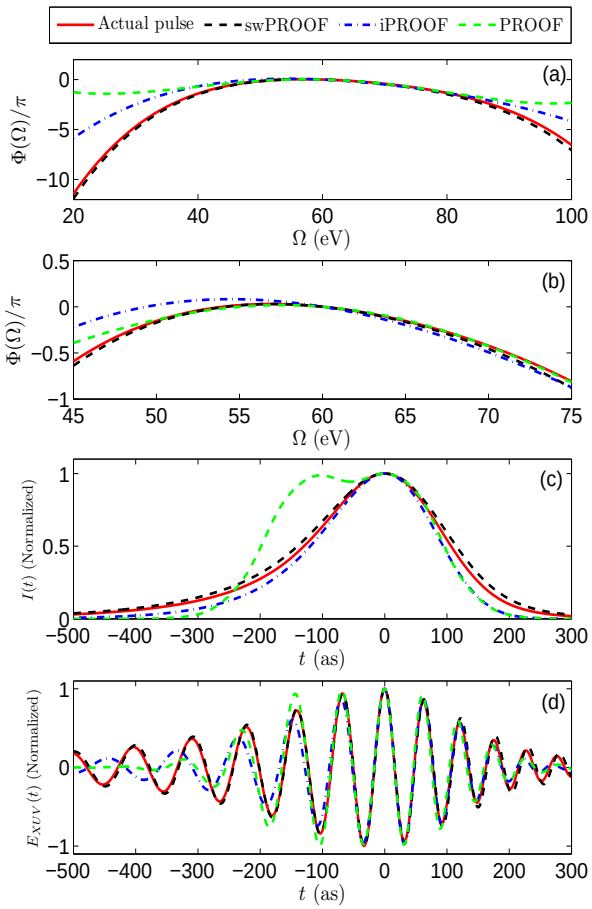

FIG. 10: (Color online) (a) the whole spectral phase (b) the spectral phase zoomed in near the central frequency (c) the normalized intensity profile in the time domain (d) the normalized electric field of the actual and retrieved XUV pulse for case1. The IR pulse used in the simulation has the following parameters: wavelength=800 nm, peak intensity=10^{11} W/cm^2, FWHM duration=8.8 fs, CEP=0, cosine-squared envelope. In the fitting procedure E_{IR} is known.

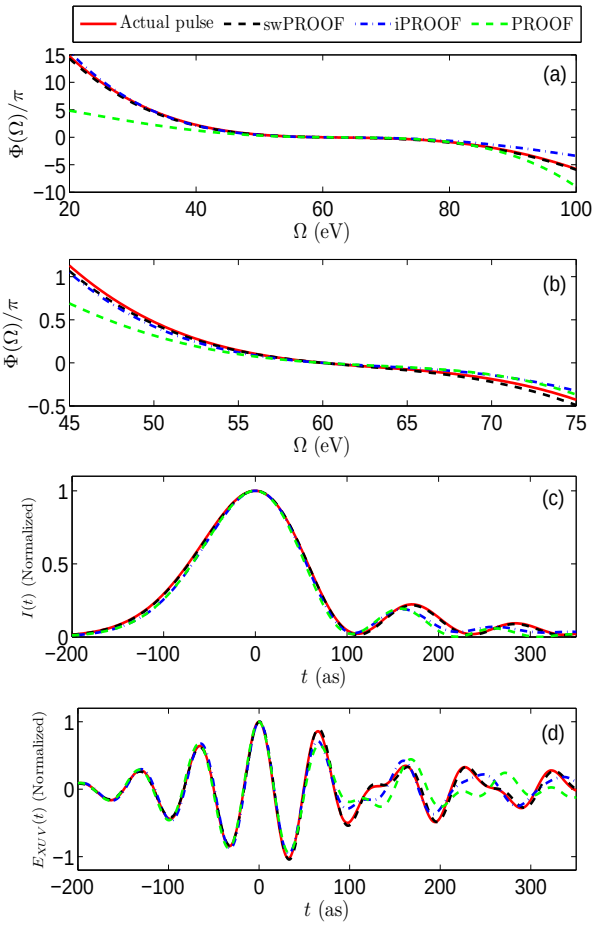

FIG. 11: (Color online) (a) the whole spectral phase (b) the spectral phase zoomed in near the central frequency (c) the normalized intensity profile in the time domain (d) the normalized electric field of the actual and retrieved XUV pulse for case2. The input IR parameters are the same as in FIG.10. In the fitting procedure E_{IR} is known.

If the IR intensity is taken as unknown when retrieving the XUV pulse, an additional freedom is added on the fitting procedure. The corresponding results are given in FIG.13 and TABLE II. From these results, overall it shows that swPROOF is more accurate and robust than iPROOF and PROOF. The iPROOF method behaves well in case1 and case2 but fails in case3 and case4, while PROOF is acceptable in case 2 and case 4 but fails in case1 and case3. Admittedly if one is looking at a single pulse parameter in a particular case alone (for example the pulse duration in case1), then one cannot say definitely that the swPROOF method is the best. However when considering all shapes and parameters of these four cases, definitely the swPROOF method is the most accurate.

case1	Actual	swPROOF	iPROOF	PROOF
XUV pulse duration (as)	235	254	235	270
XUV peak position (as)	59	62	86	63
case2	Actual	swPROOF	iPROOF	PROOF
XUV pulse duration (as)	130	129	135	122
XUV peak position (as)	89	89	91	86
case3	Actual	swPROOF	iPROOF	PROOF
XUV pulse duration (as)	103	100	118	83
XUV peak position (as)	91	97	70	48
case4	Actual	swPROOF	iPROOF	PROOF
XUV pulse duration (as)	87	84	123	88
XUV peak position (as)	-4	-7	-10	-26

TABLE II: The actual and retrieved XUV pulse parameters for case 1–4 (read from FIG.13). The IR pulse used in the TDSE simulation has a peak intensity 10^{11} W/cm^2. In the fitting procedure E_{IR} is unknown.

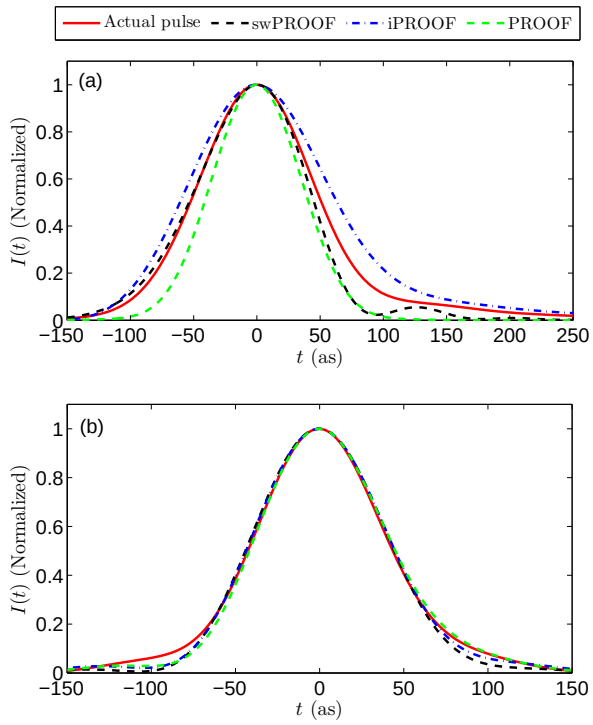

FIG. 12: (Color online) The normalized temporal intensity profile of the actual and retrieved XUV pulse for (a) case3 (b) case4. The input IR parameters are the same as in FIG.10. In the fitting procedure E_{IR} is known.

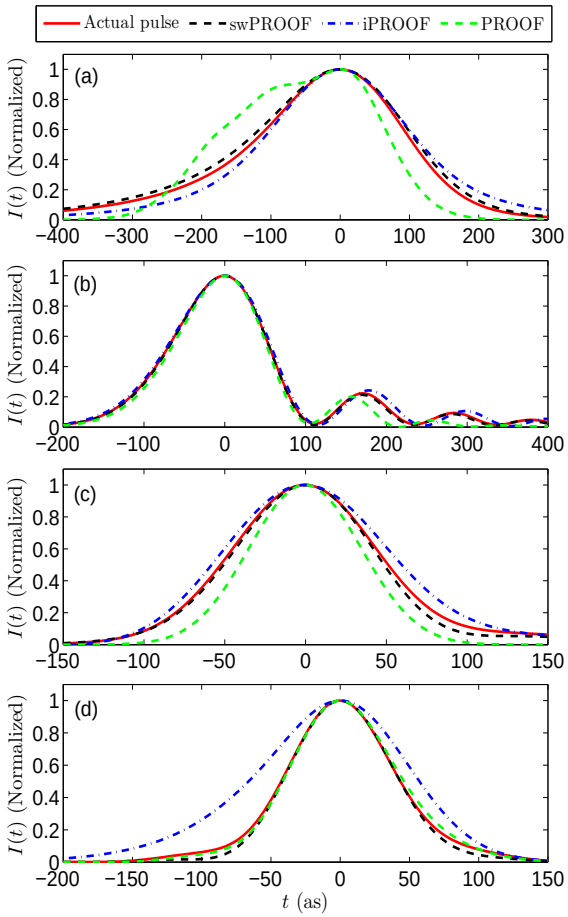

FIG. 13: (Color online) The normalized temporal intensity profile of the actual and retrieved XUV pulse for (a) case1 (b) case2 (c) case3 (d) case4. The IR pulse used in the TDSE simulation is given in the caption of FIG.10. In the fitting procedure E_{IR} is unknown.

C. Effect of the IR intensity on phase retrieval

As the dressing IR intensity increases, quantum paths involving two or more IR photons will have more contribution to the total spectrogram. Therefore the omega oscillating component S_ω extracted from the spectrogram starts to deviate from the first-second-order interference term S_{FSI} as we discussed in Sec.II.A. Such deviation will impose larger error on the pulse characterization process. FIG.14 and TABLE III show the result when the IR intensity used in the simulation was increased to 10^{12} W/cm^2. At this IR intensity the swPROOF method can still retrieve the XUV pulse successfully with the error less than 10%. FIG.15 shows the result when the dressing IR intensity increases further to 10^{13} W/cm^2. At such high intensity none of these three methods can retrieve the XUV pulse accurately, which implies the breakdown of the second-order perturbation theory.

case1	Actual	swPROOF	iPROOF	PROOF
XUV pulse duration (as)	235	227	216	217
XUV peak position (as)	59	60	84	37
case2	Actual	swPROOF	iPROOF	PROOF
XUV pulse duration (as)	130	122	125	121
XUV peak position (as)	89	85	74	83

TABLE III: The actual and retrieved XUV pulse parameters for case1 and case2 (read from FIG.14). The IR pulse used in the TDSE simulation has a peak intensity 10^{12} W/cm^2. In the fitting procedure E_{IR} is unknown.

IV. CONCLUSIONS

In this work we examined the accuracy of single attosecond pulse characterization methods. When the dressing IR field is below about 10^{12} W/cm^2, the photoelectron spectra in the XUV+IR two-color field is adequately described by the second-order perturbation theory. To "calibrate" the intrinsic accuracy of the retrieval method, we generated "experimental" photoelectron spectra with known spectral amplitude and phase of the single attosecond XUV pulses in the known IR dressing field. Adopting the PROOF and iPROOF methods to retrieve the spectral phases, we established the lack of accuracy of the spectral phases retrieved, which

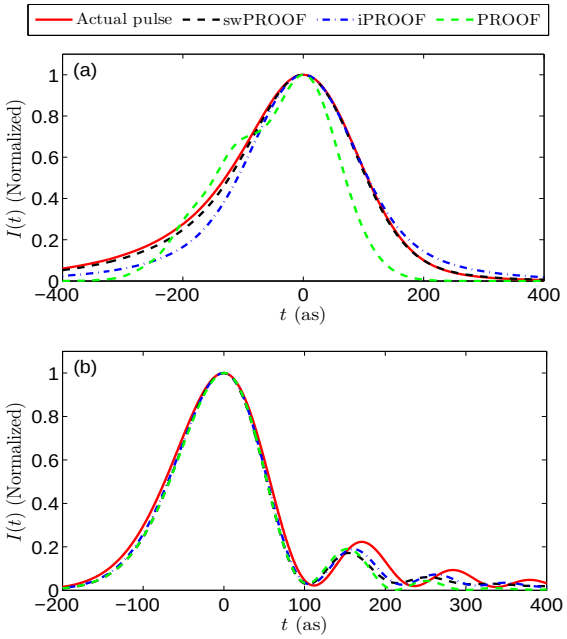

FIG. 14: (Color online) The normalized temporal intensity profile of the actual and retrieved XUV pulse for (a) case1 and (b) case2. The IR pulse used in the TDSE simulation has the following parameters: wavelength=800 nm, peak intensity=10^{12} W/cm^2, FWHM duration=8.8 fs, CEP=0, cosine-squared envelope. In the fitting procedure E_{IR} is unknown.

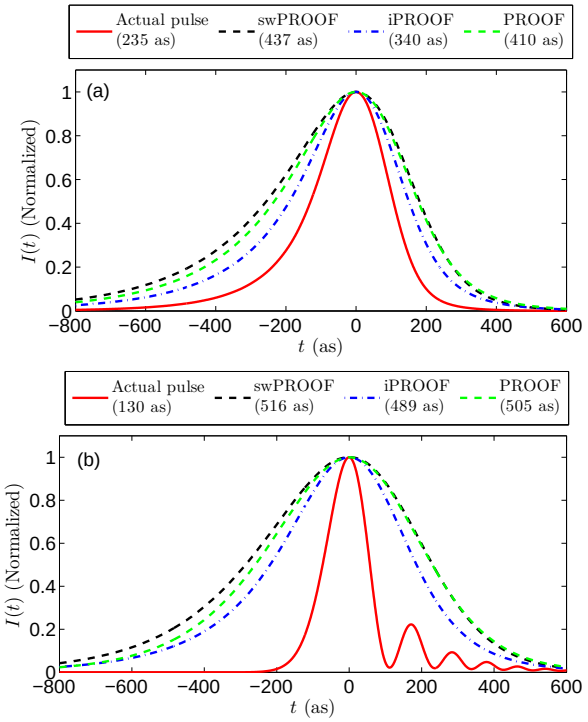

FIG. 15: (Color online) The normalized temporal intensity profile of the actual and retrieved XUV pulse for (a) case1 and (b) case2. The FWHM duration of the XUV pulse is given in the legend. The IR pulse used in the TDSE simulation has a peak intensity 10^{13} W/cm^2, other parameters are the same as in FIG.14. In the fitting procedure E_{IR} is unknown.

are then reflected in the errors of pulse duration, pulse shape and peak position in the time domain. Our results show that approximations used in PROOF and iPROOF have detrimental effects on the retrieved attosecond pulses. In the PROOF method, both first-order and 2nd-order dipole transition elements are calculated approximately. In iPROOF the 2nd-order matrix elements are approximated. These approximations are undesirable and unnecessary since theoretical tools are available for their accurate evaluations. We obtained accurate two-photon dipole matrix elements using the so-called Dalgarno-Lewis method. The modified retrieval method, which we called swPROOF, is based on an accurate theory so long that the IR intensity is constrained to below about 10^{12} W/cm^2. For attosecond pulse trains with harmonics separated by 2ω this method reduces to the familiar RABITT method. For attosecond pulse trains where harmonics are separated by ω, and for single attosecond pulses, the swPROOF method can be applied when accurate one-photon and two-photon dipole matrix elements for the target gas atoms are calculated, at least within the single active electron model. Our simulation has proven that the swPROOF method is more universal and robust than the current PROOF and iPROOF method.

The examples shown in this work demonstrate that spectral phases can be accurately retrieved from numerical "experimental" spectra calculated from solving TDSE. Using real experimental data, the accuracy will be compromised. The accuracy reported in our analysis is to be taken as the best scenario, as additional "noises" from real experimental data are added. This work shows that details of the temporal profile of attosecond pulses are very difficult to obtain exactly. This would limit the accuracy of the retrieved durations of attosecond pulses and temporal resolution in any time-domain measurements. This is not surprising since in the weak field limit, features of the photoelectron spectra are dominated by the spectral intensity. The spectral phase enters in the interference between the first and second order terms, which is only a small effect. The spectral phase is expected to show more pronounced effect at higher IR intensity, but then strong field ionization theory becomes more complicated. We note that the accuracy of the widely used FROG-CRAB method for retrieving spectral phases has not been carefully examined through TDSE simulation yet.

Looking ahead, attosecond pulses in the water-window region and beyond will be generated with mid-infrared lasers in the near future. Will the swPROOF method still be the method for characterizing such attosecond pulses? At higher photon energies the atomic parameters are nor-

mally less important, but electrons from multiple inner shells are generated. Helium is the only target that does not have this complication, but its photoionization cross section is notoriously smaller. While high-order harmonics have been reported way beyond 150 eV with mid-infrared lasers, attosecond pulses at these energies still have not been reported. Clearly characterization of such attosecond pulses in the time domain is an important issue that has to be faced in theory and in experiments.

Acknowledgments

This research was supported by Chemical Sciences, Geosciences and Biosciences Division, Office of Basic Energy Sciences, Office of Science, U.S. Department of Energy. Some of the computation was performed on the Beocat Research Cluster at Kansas State University. T. Morishita is supported in part by the Grants-in-Aid for scientific research (A), (B), and (C) from the Japan Society for the Promotion of Science.

[1] P. M. Paul, E. S. Toma, P. Breger, G. Mullot, F. Augé, Ph. Balcou, H. G. Muller and P. Agostini, Science **292**, 1689 (2001).
[2] M. Hentschel *et al.*, Nature **414**, 509 (2001).
[3] E. Goulielmakis *et al.*, Science **320**, 1614 (2008).
[4] K. Zhao, Q. Zhang, M. Chini, Y. Wu, X. Wang and Z. Chang, Opt. Lett. **37**, 3891 (2012).
[5] I. J. Sola *et al.*, Nature Phys. **2**, 319 (2006).
[6] H. Mashiko, S. Gilbertson, C. Li, S. D. Khan, M. M. Shakya, E. Moon and Z. Chang, Phys. Rev. Lett. **100**, 103906 (2008).
[7] H. Vincenti and F. Quéré, Phys. Rev. Lett. **108**, 113904 (2012).
[8] K. T. Kim, C. Zhang, T. Ruchon, J. F. Hergott, T. Auguste, D. M. Villeneuve, P. B. Corkum and F. Quéré, Nature Photonics **7**, 651 (2013).
[9] C. M. Heyl, S. N. Bengtsson, S. Carlström, J. Mauritsson, C. L. Arnold and A. L'Huillier, New Journal of Physics **16**, 052001 (2014).
[10] M. Chini, K. Zhao and Z. Chang, Nature Photonics **8**, 178 (2014).
[11] M. Drescher *et al.*, Nature **419**, 803 (2002).
[12] M. Uiberacker *et al.*, Nature **446**, 627 (2007).
[13] A. L. Cavalieri *et al.*, Nature **449**, 1029 (2007).
[14] E. Gagnon, P. Ranitovic, X. M. Tong, C. L. Cocke, M. M. Murnane, H. C. Kapteyn and A. S. Sandhu, Science **317**, 1374 (2007).
[15] F. Krausz and M. Ivanov, Rev. Mod. Phys. **81**, 163 (2009).
[16] E. Goulielmakis *et al.*, Nature **466**, 739 (2010).
[17] J. Mauritsson *et al.*, Phys. Rev. Lett. **105**, 053001 (2010).
[18] M. Schultze *et al.*, Science **328**, 1658 (2010).
[19] K. Klünder *et al.*, Phys. Rev. Lett. **106**, 143002 (2011).
[20] P. Tzallas, E. Skantzakis, L. A. A. Nikolopoulos, G. D. Tsakiris and D. Charalambidis, Nature Phys. **7**, 781 (2011).
[21] G. Wu, P. Hockett and A. Stolow, Phys. Chem. Chem. Phys. **13**, 18447 (2011).
[22] D. Guénot *et al.*, Phys. Rev. A **85**, 053424 (2012).
[23] X. H. Xie *et al.*, Phys. Rev. Lett. **109**, 243001 (2012).
[24] G. Laurent, W. Cao, H. Li, Z. Wang, I. Ben-Itzhak and C. L. Cocke, Phys. Rev. Lett. **109**, 083001 (2012).
[25] Ch. Neidel *et al.*, Phys. Rev. Lett. **111**, 033001 (2013).
[26] D. Mendive-Tapia, M. Vacher, M. J. Bearpark and M. A. Robb, J. Chem. Phys. **139**, 044110 (2013).
[27] K. T. Kim, D. M. Villeneuve and P. B. Corkum, Nature Photonics **8**, 187 (2014).
[28] M. J. J. Vrakking, Phys. Chem. Chem. Phys. **16**, 2775 (2014).
[29] Z. H. Loh, C. H. Greene and S. R. Leone, Chem. Phys. **350**, 7 (2008).
[30] H. Wang, M. Chini, S. Chen, C. H. Zhang, Y. Cheng, F. He, Y. Wu, U. Thumm and Z. Chang, Phys. Rev. Lett. **105**, 143002 (2010).
[31] M. Chini, B. Zhao, H. Wang, Y. Cheng, S. X. Hu and Z. Chang, Phys. Rev. Lett. **109**, 073601 (2012).
[32] M. B. Gaarde, C. Buth, J. L. Tate and K. J. Schafer, Phys. Rev. A **83**, 013419 (2011).
[33] S. Pabst, A. Sytcheva, A. Moulet, A. Wirth, E. Goulielmakis and R. Santra, Phys. Rev. A **86**, 063411 (2012).
[34] M. Lin, A. N. Pfeiffer, D. M. Neumark, S. R. Leone and O. Gessner, J. Chem. Phys. **137**, 244305 (2012).
[35] F. Lépine, M. Y. Ivanov and M. J. J. Vrakking, Nature Photonics **8**, 195 (2014).
[36] Y. Mairesse *et al.*, Science **302**, 1540 (2003).
[37] E. Cormier, I. A. Walmsley, E. M. Kosik, A. S. Wyatt, L. Corner and L. F. DiMauro, Phys. Rev. Lett. **94**, 033905 (2005).
[38] Y. Ge, Phys. Rev. A **77**, 033851 (2008).
[39] H. Wang, M. Chini, S. D. Khan, S. Chen, S. Gilbertson, X. Feng, H. Mashiko and Z. Chang, J. Phys. B **42**, 134007 (2009).
[40] W. Cao, G. Laurent, C. Jin, H. Li, Z. Wang, C. D. Lin, I. Ben-Itzhak and C. L. Cocke, J. Phys. B **45**, 074013 (2012).
[41] K. T. Kim *et al.*, Nature Phys. **9**, 159 (2013).
[42] J. Itatani, F. Quéré, G. L. Yudin, M. Yu. Ivanov, F. Krausz and P. B. Corkum, Phys. Rev. Lett. **88**, 173903 (2002).
[43] M. Kitzler, N. Milosevic, A. Scrinzi, F. Krausz and T. Brabec, Phys. Rev. Lett. **88**, 173904 (2002).
[44] Y. Mairesse and F. Quéré, Phys. Rev. A **71**, 011401 (2005).
[45] J. Gagnon, E. Goulielmakis and V. S. Yakovlev, Appl. Phys. B **92**, 25 (2008).
[46] G. L. Yudin, S. Patchkovskii and A. D. Bandrauk,

J. Phys. B **41**, 045602 (2008).
[47] V. S. Yakovlev, J. Gagnon, N. Karpowicz and F. Krausz, Phys. Rev. Lett. **105**, 073001 (2010).
[48] G. Laurent, W. Cao, I. Ben-Itzhak and C. L. Cocke, Opt. Express **21**, 16914 (2013).
[49] M. Chini, S. Gilbertson, S. D. Khan, and Z. Chang, Opt. Express **18**, 13006 (2010).
[50] J. M. Dahlström, A. L'Huillier and A. Maquet, J. Phys. B **45**, 183001 (2012).
[51] J. M. Dahlström, D. Guénot, K. Klünder, M. Gisselbrecht, J. Mauritsson, A. L'Huillier, A. Maquet and R. Taïeb, Chem. Phys. **414**, 53 (2013).
[52] A. Dalgarno and J. T. Lewis, Proc. R. Soc. A **233**, 70 (1955).
[53] X. M. Tong and C. D. Lin, J. Phys. B **38**, 2593 (2005).
[54] J. M. Dahlström and E. Lindroth, J. Phys. B **47**, 124012 (2014).
[55] C. Liu, M. Reduzzi, A. Trabattoni, A. Sunilkumar, A. Dubrouil, F. Calegari, M. Nisoli and G. Sansone, Phys. Rev. Lett. **111**, 123901 (2013).
[56] M. Aymar and M. Crance, J. Phys. B **13**, L287 (1980).
[57] E. S. Toma and H. G. Muller, J. Phys. B **35**, 3435 (2002).
[58] J. W. Cooper, Phys. Rev. **128**, 681 (1962).
[59] A. Maquet and R. Taïeb, J. Mod. Opt. **54**, 1847 (2007).
[60] A. J. Galán, L. Argenti and F. Martín, New Journal of Physics **15**, 113009 (2013).
[61] E. P. Wigner, Phys. Rev. **98**, 145 (1955).
[62] F. T. Smith, Phys. Rev. **118**, 349 (1960).
[63] Misha Ivanov and Olga Smirnova, Phys. Rev. Lett. **107**, 213605 (2011).
[64] S. Nagele, R. Pazourek, J. Feist and J. Burgdörfer, Phys. Rev. A **85**, 033401 (2012).
[65] J. M. Dahlström, T. Carette and E. Lindroth, Phys. Rev. A **86**, 061402 (2012).
[66] D. Guénot *et al.*, J. Phys. B **47**, 245602 (2014).
[67] Z. Chen, T. Morishita, A. T. Le, M. Wickenhauser, X. M. Tong, and C. D. Lin, Phys. Rev. A **74**, 053405 (2006).
[68] T. Morishita, Z. Chen, S. Watanabe and C. D. Lin, Phys. Rev. A **75**, 023407 (2007).
[69] J. Xu, Z. Chen, A. T. Le and C. D. Lin, Phys. Rev. A **82**, 033403 (2010).
[70] D. L. Carroll, "FORTRAN genetic algorithm driver", 1999, http://cuaerospace.com/carroll/ga.html (accessed in May 2008).